Topological phases in pseudospin-1 Fermi gases with two-dimensional spin-orbit coupling

Junpeng Hou, Haiping Hu, and Chuanwei Zhang[*]

Department of Physics, The University of Texas at Dallas, Richardson, Texas 75080, USA

The recent experimental realization of spin-orbit (SO) coupling for ultracold bosons and fermions opens an exciting avenue for engineering quantum matter that may be challenging to realize in solid-state materials such as SO-coupled pseudospin-1 fermions. While one-dimensional SO coupling for spin-1 bosons has been experimentally realized, the generation of two-dimensional (2D) SO coupling and its topological properties are largely unexplored. Here we propose an experimental scheme for realizing a 2D Rashba-type SO coupling in a square lattice for pseudospin-1 Fermi gases. Because of the extended spin degree of freedom, many interesting topological phases could exist without relying on lattice point group symmetries that are crucial in solid-state materials. These exotic phases include triply degenerate points, quadratic band touching, a large Chern number ($C = 5$) superfluid with five Majorana modes, triple-Weyl fermions, and so on. Our scheme can be generalized to larger spins and provides a distinctive route for engineering topological quantum matter by utilizing large spin degrees of freedom, instead of specific lattice symmetries.

I. INTRODUCTION

Spin-orbit (SO) coupling, the interaction between spin and orbital (e.g., momentum) degrees of freedom of a particle, plays an important role in many topological phases of matter. In ultracold atomic gases, synthetic SO coupling has been realized by coupling atomic hyperfine ground states (denoted as pseudospins, but sometimes abbreviated as spin if there is no ambiguity) using Raman lasers that induce momentum changes between different spin states. In particular, both (one-dimensional) 1D and two-dimensional (2D) SO couplings have been realized in experiments for pseudospin-1/2 bosons and fermions and their distinct properties have been widely studied [1–12].

Recently, 1D SO coupling for spin-1 bosons has also been experimentally realized [13,14], which hosts some interesting quantum phases [15–20]. Different from the electron's spin-1/2, the large number of available hyperfine states provide a platform for studying fermionic atoms with integer pseudospins such as pseudospin-1, which generally are difficult to realize in solid-state materials. The existence of such extra spin states naturally poses two important questions: Can important topological physics emerge from 2D SO-coupled pseudospin-1 Fermi gases? If so, how can pseudospin-1 2D SO coupling be realized in realistic experimental systems?

In this paper, we address these two important questions by showing that many exotic topological phases can emerge from a pseudospin-1 degenerate Fermi gas in a square optical lattice with 2D Rashba-type SO coupling, which can be realized with a simple laser setup. These topological phases originate from the coupling with the extra spin state in spin-1, instead of certain lattice symmetries that dictate many topological solid-state materials. Our main results are as follows.

(i) In the absence of Zeeman field to lift the degeneracy of three pseudospin states at the center of the Brillouin zone (BZ), there exists a single triply degenerate point in the 2D single-particle band structure, which consists of two linear and one flat bands. Three-dimensional triply degenerate points have been theoretically proposed in solid-state, ultracold atomic, and optical systems with some experimental evidences [21–29]. The 2D triply degenerate point here resembles a Dirac point in graphene without the valley degree of freedom [30]. A spin-tensor Zeeman field breaks the triple degeneracy, leading to a quadratic band touching point due to indirect second-order spin coupling. Quadratic band touching points have attracted great attention recently due to their nonlinear dispersions [31–33] and many-body interaction-driven quantum anomalous Hall ground states with time-reversal symmetry breaking [31,32,34–37].

(ii) In the presence of attractive s-wave pairing interaction, 2D superfluids can become topological with large Chern numbers up to ± 5. The topological phase transition between different phases can be accompanied with the band gap closing at (up to two) points with cubic band touching through pairing and indirect spin coupling, yielding the largest Chern number change of 6. The large Chern number topological superfluid can host up to five Majorana edge states [38–40] simultaneously at the boundary.

(iii) In a 3D superfluid with 2D SO coupling, each cubic band touching point becomes two triple-Weyl nodes located at $\pm k_z$ due to the change of the effective chemical potential through the kinematic energy $\sim k_z^2$. Multi-Weyl fermions have attracted great attention due to their multiple monopole charges and unusual transport properties in solid-state materials [41–46].

*chuanwei.zhang@utdallas.edu

(iv) An experimental setup for realizing 2D Rashba-type SO coupling for pseudospin-1 atomic gases is proposed based on recently experimental success for realizing 2D SO coupling for pseudospin-1/2 atoms [10].

(v) Extending the findings to a higher pseudospin s, we show that a high-order band touching point at the order of $2s$ and $4s - 1$ can exist for single-particle bands and pairing superfluids, respectively.

II. HAMILTONIAN AND SINGLE-PARTICLE BAND TOPOLOGY

We consider a Rashba-type SO-coupled pseudospin-1 Fermi gas confined in a square lattice with both vector (linear) and tensor (quadratic) Zeeman fields. The single-particle Hamiltonian in the momentum space can be written as

$$H_0 = -d_x F_x - d_y F_y + d_z \left(I - \tfrac{1}{2} F_z^2\right) + \tfrac{1}{2} \delta_V F_z + \tfrac{1}{4} \delta_T F_z^2, \quad (1)$$

under the three spin basis $\{|1\rangle, |0\rangle, |-1\rangle\}$, where $d_x = 2t_{so} \sin(k_y)$, $d_y = 2t_{so} \sin(k_x)$, $d_z = 2t[\cos(k_x) + \cos(k_y)]$, F_i represent the spin-1 vector operators. They can be expressed as $[F_x]_{mm'} = \sqrt{2}(\delta_{m-1,m'} + \delta_{m+1,m'})$, $[F_y]_{mm'} = \sqrt{2}i(\delta_{m-1,m'} - \delta_{m+1,m'})$, and $[F_z]_{mm'} = 2m\delta_{m,m'}$ (see Appendix A). δ_T and δ_V denote the tensor and vector Zeeman fields. The experimental scheme for realizing this Hamiltonian will be discussed later in the paper. Hereafter we take $t = t_{so} = 1$ for simplicity of the presentation.

When the vector Zeeman field $\delta_V = 0$, the time-reversal symmetry of the system is preserved. In this region, when the tensor Zeeman field $\delta_T = \pm 8$ or 0, one (at the Γ or M point) or two (at X points) 2D triply degenerate points appear in the band structure, each of which carries a topological charge (winding number) -2. An example of the triply degenerate point at Γ point for $\delta_T = 8$ is plotted in Fig. 1(a). The low-energy effective Hamiltonian around Γ is $\sim -(k_y F_x + k_x F_y)$ up to some constants, which can be taken as a natural extension of the spin-1/2 Rashba SO coupling $k_y \sigma_x + k_x \sigma_y$ (σ_i, $i = x, y, z$ are Pauli matrices).

The triple degeneracy at Γ for $\delta_T = 8$ can be lifted by varying δ_T and δ_V. When the time-reversal symmetry is still preserved (i.e., $\delta_V = 0$), the decrease of δ_T disappears from the top band, leaving a quadratic band touching between two bottom bands [Fig. 1(b)]. The physics around the quadratic band touching point can be described by an effective Hamiltonian $H_\Gamma = -2k_y F_x - 2k_x F_y + (\delta_T - 8)F_z^2/4$, where two degenerate spin states $|1\rangle$ and $|-1\rangle$ at $\mathbf{k} = 0$ are indirectly coupled through $|0\rangle$. Near the origin $\mathbf{k} = 0$, the effective two-level Hamiltonian (up to the second order) becomes

$$H_{QBT} = -2\left(k_x^2 - k_y^2\right)\sigma_x - 4k_x k_y \sigma_y + 2\left(k_x^2 + k_y^2\right)I \quad (2)$$

for two touched bands. Such quadratic band touching has a winding number -2.

The Hamiltonian (2) is similar to that for a quadratic band touching in checkerboard (C_4) and Kagome (C_6) lattices, which requires time-reversal symmetry and the corresponding point group symmetry to be topologically robust [32]. In contrast, the quadratic band touching in our model is only protected by time-reversal symmetry and robust to the breaking of C_4 rotational symmetry because it stems from the indirect coupling induced by extra spin degrees of freedom, as
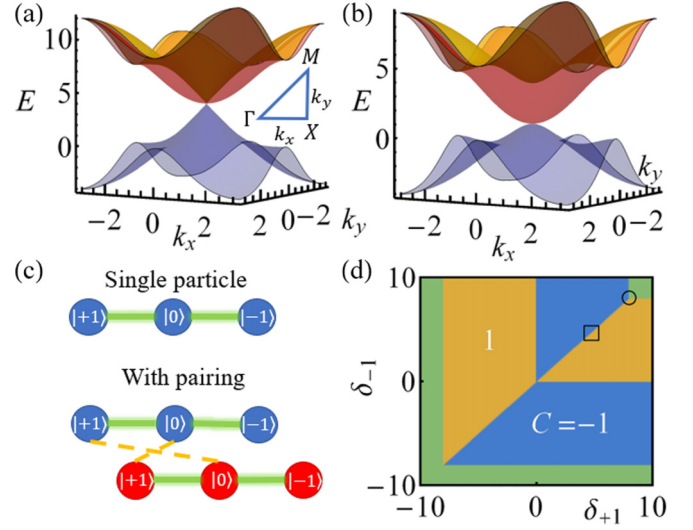

FIG. 1. (a) A 2D triply degenerate point carrying -2π Berry phase locates at Γ point for $\delta_T = 8$ and $\delta_V = 0$. A quadratic band touching appears at X/M points for two upper bands. Inset shows high-symmetry points in the BZ for a square lattice. (b) Two quadratic band touchings located at Γ (between two lower bands) and X/M (two upper bands) points for $\delta_T = 5$ and $\delta_V = 0$. (c) Coupling scheme with/without superfluid pairing. The green line represents SO coupling, which contributes a winding number -1. The dashed yellow line represents the s-wave pairing, which does not contribute any winding. The blue and red branches correspond to particles and holes. (d) Phase diagram of Chern number for the lower band. The circle and square denote the parameters for (a) and (b), respectively.

illustrated in Fig. 1(c). The green lines represent SO coupling $-\sin(k_y) + i\sin(k_x)$, which contributes a winding ± 1 at different high-symmetry points. When two spins $|1\rangle$ and $|-1\rangle$ are degenerate, their touching point would naturally possess a winding number ± 2 and exhibit quadratic band touching. Nevertheless, due to the lack of point group symmetries in its mechanism, the quadratic band touching here cannot be split into several Dirac cones. Upon breaking time-reversal symmetry through a vector Zeeman field δ_V, a gapped phase with nontrivial Chern numbers for each band appears (see Appendix B).

Hereafter we use the detunings $\delta_{\pm 1} = \delta_T \pm \delta_V$ for spin states $|\pm 1\rangle$ from $|0\rangle$, which are more relevant to realistic experimental parameters. The single-particle phase diagram for the lowest band is shown in Fig. 1(d). In the gapped phase regions, the band Chern numbers are nonzero as long as $|\delta_{+1}| < 8$ or $|\delta_{-1}| < 8$. More details about the single-particle phase diagram are presented in Appendix B.

III. LARGE CHERN NUMBER 2D SUPERFLUIDS

We consider a two-body s-wave attractive interaction between Fermionic atoms. In experiments, the interaction between different spin states can be tuned by Feshbach resonance [47,48]. Here we assume, without loss of generality, that the interaction $-\sum_i U_{+1,0} n_{i,+1} n_{i,0}$ between spins $|+1\rangle$ and $|0\rangle$ is tuned to be dominant, where $\mathbf{i} = (i_x, i_y)$ is the 2D lattice-site index, $\hat{n}_{i,\sigma} = \hat{c}_{i,\sigma}^\dagger \hat{c}_{i,\sigma}$ is the particle number operator and $U_{+1,0} > 0$ is the interaction strength.
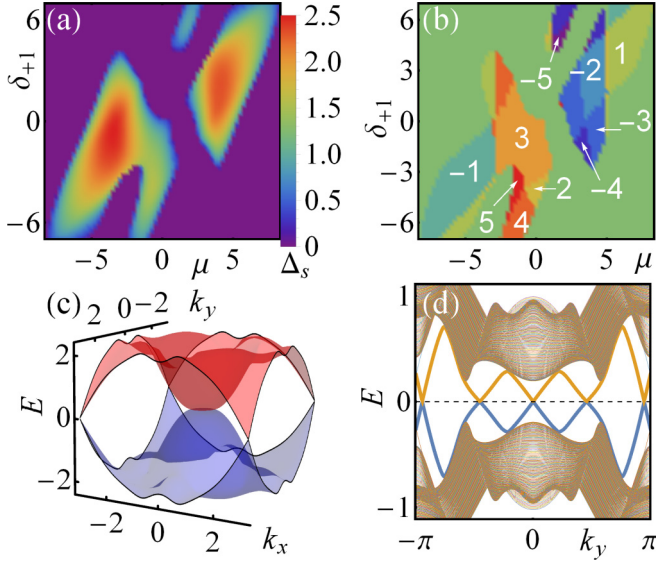
FIG. 2. (a, b) The phase diagrams of order parameter and Chern number with respect to δ_{+1} and μ for $\delta_{-1} = 1$. The Chern number is summed over the hole branch and vanishes with the zero order parameter. (c) Coexistence of a cubic band touching and a Dirac point in BZ. $\delta_{+1} = -2$, $\delta_{-1} = 1$, and $\mu = -3$. (d) Quasiparticle spectrum with an open-boundary condition along the x direction. $\delta_{+1} = -4.5$, $\delta_{-1} = 1$, and $\mu = -1.5$.

Under the mean-field approach, the Bogoliubov–de Gennes (BdG) Hamiltonian for the 2D superfluid can be written as

$$H_\Delta = -d_x F_x \otimes \tau_I - d_y F_y \otimes \tau_z + d_z \left(I - 2F_z^2\right) \otimes \tau_z$$
$$+ \left(\delta_T F_z^2 + \delta_V F_z - \mu I\right) \otimes \tau_z + (\Delta_s F_s \otimes \tau_+ + \text{H.c.}),$$
$$(3)$$

in the Nambu basis $\Psi_{\boldsymbol{k}} = (\hat{c}_{\boldsymbol{k},+1}, \hat{c}_{\boldsymbol{k},0}, \hat{c}_{\boldsymbol{k},-1}, \hat{c}^\dagger_{-\boldsymbol{k},+1}, \hat{c}^\dagger_{-\boldsymbol{k},0}, \hat{c}^\dagger_{-\boldsymbol{k},-1})$, where μ is the chemical potential, τ_I and τ_i are the identity matrix and Pauli matrices acting on Nambu space, $F_s = i(F_y + \{F_y, F_z/2\})$, and the s-wave superfluid order parameter $\Delta_s = (U_{+1,0}/N_0) \sum_{\boldsymbol{k}} \langle \hat{c}_{\boldsymbol{k},+1} \hat{c}_{-\boldsymbol{k},0} \rangle$ with N_0 the number of atoms in spin states $|+1\rangle$ and $|0\rangle$. Despite that such a pairing breaks time-reversal symmetry, the particle-hole symmetry $\mathcal{P} = \tau_x \widehat{K}$ is still preserved. The order parameter is self-consistently determined by minimizing the thermodynamical potential [49,50] and the corresponding phase diagram at $\delta_{-1} = 1$ is plotted in Figs. 2(a) and 2(b).

The coupling between different states in the above BdG Hamiltonian is illustrated in Fig. 1(c), where the blue and red branches denote particles and holes. The dashed yellow lines are couplings through order parameter Δ_s, which do not contribute any winding. The highest-order band touching is then cubic, which is given by the indirect coupling between particles and holes at spin state $|-1\rangle$. Moreover, different types of band touching may appear at different high-symmetry points at the same time. In Fig. 2(c), we show a gapless phase with both cubic band touching at Γ and Dirac-type linear touching at the M point.

In the numerical phase diagram of the 2D superfluid [Figs. 2(a) and 2(b)], a large Chern number up to ± 5 appears
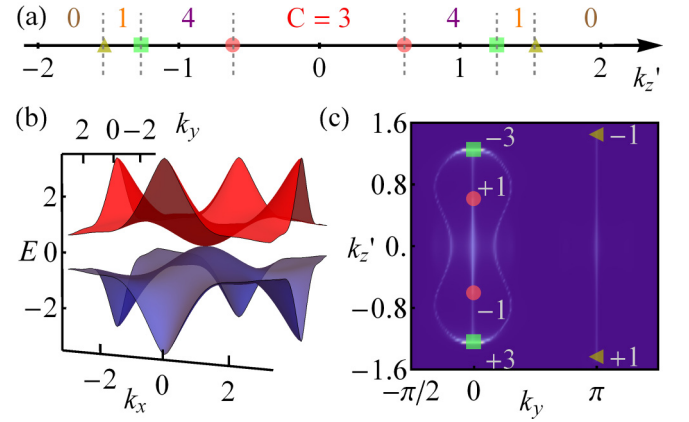

FIG. 3. Triple-Weyl node in a 3D topological superfluid. (a) Change of the 2D band Chern number with respect to k_z' due to the change of the effective chemical potential μ_{eff}. Green square, red disk, and yellow triangle denote a triple-Weyl node that locate at Γ in the (k_x, k_y) plane, a Weyl point at Γ, and a Weyl point at M, respectively. (b) Plot of the triple-Weyl node in 2D BZ at $k_z' = 1.26$, which shows cubic band dispersion along both k_x and k_y. (c) Surface spectral densities and Fermi arcs in the k_y-k_z' surface plane with $\omega = 0$. $\delta_{+1} = 2$, $\delta_{-1} = 1$, and $\mu = -1.4$.

while the change of Chern number may reach 6 (from 1 to -5), which is achieved through two cubic-band crossings. The effective two-level Hamiltonian around a Γ cubic-band touching point is $\sim -(k_y^3 - 3k_x^2 k_y)\sigma_x - (k_x^3 - 3k_x k_y^2)\sigma_y + (k_x^2 + k_y^2)\sigma_z$. In the gapped region, multiple Majorana edge states emerge for the large Chern number 2D superfluid. In Fig. 2(d), we plot the band structure for a topological superfluid with Chern number 5 under the open boundary condition along x and periodic boundary condition along y. Clearly five Majorana edge states appear at each edge in the superfluid band gap.

IV. TRIPLE-WEYL NODES IN 3D SUPERFLUIDS

We consider a 3D superfluid with the same 2D SO coupling and free dispersion along the k_z direction. Because k_z only enters the Hamiltonian through the kinetic energy, we can incorporate it by replacing the chemical potential μ in the BdG Hamiltonian (3) with the effective chemical potential $\mu_{\text{eff}} = \mu - \hbar^2 k_z^2/(2m)$. For convenience, we use the coordinate $k_z' = (\hbar/\sqrt{2m})k_z$. An example of the change of the 2D band topology with k_z' is shown in Fig. 3(a). At $k_z' = 0$, the 2D Chern number is 3 for the chosen chemical potential μ. With increasing $k_z'^2$, μ_{eff} decreases, leading to band-gap closing at different points and the change of Chern number, as shown in Figs. 2(b) and 2(c). Such band-gap closing points yield linear or multi-Weyl nodes in 3D momentum space. In total, there are three types of band touchings at different k_z' and they are labeled with differently colored shapes in Figs. 3(a) and 3(c). Unlike multi-Weyl nodes in electronic systems, here the Weyl points are not protected by C_n point-group symmetry, therefore we may have triple-Weyl nodes even though our model itself exhibits only C_4, instead of C_6 symmetry [41]. Such a triple-Weyl node shows a cubic-band dispersion in the k_x-k_y plane [Fig. 3(b)] and is linear along the k_z direction
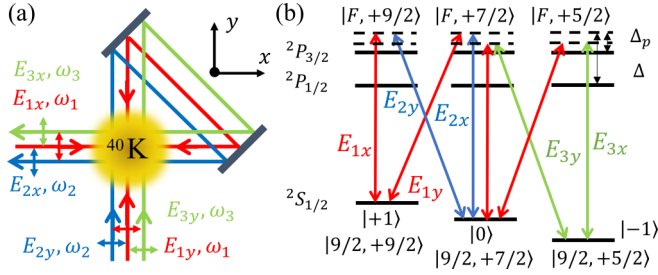
FIG. 4. (a) Experimental scheme for implementing 2D Rashba-type SO coupling in fermion atoms ^{40}K using a standing wave $\boldsymbol{E}_{1x(z)}$ and two plane-wave $\boldsymbol{E}_{2(3)x(z)}$ laser fields. The arrows indicate the directions of corresponding beams and each beam is reflected by two mirrors (dark gray lines). (b) Level diagram and optical coupling in the hyperfine structure $|F, m\rangle$ of ^{40}K atoms.

(see Appendix C). By keeping only the leading order, the two-level low-energy Hamiltonian around the Weyl point is $\sim -(k_y^3 - 3k_x^2 k_y)\sigma_x - (k_x^3 - 3k_x k_y^2)\sigma_y + k'_z \sigma_z$ up to some constants, which is the same as that stabilized by the C_6 point group in topological semimetals [41].

To characterize the surface states and the triple-Weyl nodes in Fig. 3(b), we calculate and plot the spectral density function $A(\omega, \mathbf{k}) = \text{Im}G(i\omega, \mathbf{k})/\pi$ at $\omega = 0$ in Fig. 3(c) with an open boundary condition along the x direction, where $G(i\omega, \mathbf{k})$ is the single-particle Green's function. We also shift the BZ to make all surface Fermi arcs visible. The pair of Weyl points at M (yellow triangle) gives an isolated surface arc at $k_y = \pi$. The surface arc connecting Γ Weyl points (red disks) overlaps with one of the three Fermi arcs connecting the Γ triple-Weyl nodes (green square) at $k_y = 0$, therefore the density is slightly higher.

We remark that because the multi-Weyl nodes here do not rely on the existence of point group symmetries C_n, they are also robust to the breaking of C_4 symmetry, which is preserved by the system Hamiltonian. For electronic materials with orbital degree of freedom, the highest order for a multi-Weyl node is triple because it is stabilized through C_6 symmetry, which is the highest order allowed by classical crystalline order. In contrast, a quadruple-Weyl or quintuple-Weyl node can be found, in principle, in a spin-3/2 system.

V. FURTHER DISCUSSIONS

A. Experimental scheme for generating 2D SO coupling

We briefly illustrate the experimental proposal for implementing 2D SO coupling in the Hamiltonian Eq. (1), which could be considered as a natural generalization of the experimentally realized 2D SO coupling for spin-1/2 atoms [10,51]. The scheme is presented using ^{40}K atoms, but a similar setup could apply to ^{173}Yb [52,53] or ^{161}Dy [54] atoms, which have much less heating from Raman lasers. More details are provided in Appendix D. Our proposal focuses on lattice systems while the realization of the spin-orbit coupling in free space [8,9,12] may enable the generalization and study of these distinctive band touchings in free space.

The basic experimental setup is shown in Fig. 4(a). Two counterpropagating Raman lasers (red) form standing wave fields $\boldsymbol{E}_{1x} = \hat{z}E_{1x}\cos(k_0 x)$ and $\boldsymbol{E}_{1z} = \hat{x}E_{1z}\cos(k_0 z)$ along the

x and z directions, which also generate a spin-independent square lattice $V(\boldsymbol{r}) = V_{0x}\cos^2(k_0 x) + V_{0z}\cos^2(k_0 z)$. As illustrated in Fig. 4(b), the red standing wave and blue plane wave $\boldsymbol{E}_{2x} = \hat{z}E_{2x}e^{ik_0 x}$, $\boldsymbol{E}_{2z} = \hat{x}E_{2z}e^{ik_0 z}$ (or green plane wave $\boldsymbol{E}_{3x} = \hat{z}E_{3x}e^{ik_0 x}$, $\boldsymbol{E}_{3z} = \hat{x}E_{3z}e^{ik_0 z}$) can induce a two-photon Raman transition between $|+1\rangle$ and $|0\rangle$ (or $|0\rangle$ and $|-1\rangle$). The resulting Raman coupling can be written as $\sim M_x(x, z)F_x + M_y(x, z)F_y$ in the spin-1 basis with $M_x(x, z) = -M_{0x}\cos(k_0 x)\sin(k_0 z)$ and $M_y(x, z) = -M_{0y}\sin(k_0 z)\cos(k_0 x)$, which yield the 2D SO coupling $d_x F_x + d_y F_y$ in the Hamiltonian [Eq. (1)] under the tight-binding approximation (in the x-z plane). The coupling strength $M_{0x(y)}$ can be tuned through the intensity of Raman beams and optical detunings Δ_s and Δ_p. In the lattice model, the bands between $|\pm 1\rangle$ and $|0\rangle$ are inverted, yielding the term $d_z(I - F_z^2/2)$ in Eq. (1). The tensor and vector Zeeman fields $\delta_T F_z^2/4 + \delta_V F_z/2$ can be tuned by changing the two-photon Raman detunings $\delta_{\pm 1}$ between $|\pm 1\rangle$ and $|0\rangle$. The s-wave pairing interaction can be tuned through Feshbach resonance [5,47,48]. To observe the topological edge state, the previous experimental scheme of quenching a shaping potential in 2D a square lattice can be similarly implemented [55].

B. Extension to a larger spin

Both the physical results and proposed experimental scheme can be extended to even higher spin systems. Here we simply list the results and leave the details in Appendix E. We consider a spin-s system, where only neighboring spins are coupled through Rashba- or Rashba-type SO coupling and each coupling term may contribute a winding number ± 1. At a certain high-symmetry point in BZ, two bands may become degenerate and a high-order band crossing point appears with large Berry flux. Specifically, if the band touching has an mth-order dispersion relation, it can possess a winding number m, $m - 2,..., -m + 2$ and $-m$, depending on the explicit form of the system Hamiltonian. Based on this argument, there are two types of quadratic band touchings, one with ± 2 winding and the other is trivial. The low-energy Hamiltonian for the later can be written as $k_y F_x \pm k_x\{F_y, F_z\}$. There are totally $2s$ SO coupling terms, therefore the highest-order band touching should have a winding number $\pm 2s$. Moreover, when multiple bands become degenerate at one single momentum, we would have a topologically nontrivial and more complicated counterpart of the triply degenerate point.

When the s-wave attractive pairing interaction is considered, the highest-order band crossing in the superfluid phase has the order $4s - 1$ because the order parameter does not contribute any winding and the pairing only occurs between different spin states. The extension to a multi-Weyl node with a maximum $4s - 1$ charge in a 3D superfluid is apparent. All those exotic types of band touching points do not require any specific symmetries like point group or inversion symmetries, but they still can be topologically nontrivial (they do require time-reversal symmetry in certain cases like the quadratic band touching discussed here). Therefore the large spin systems have significant advantages over the usual spin-1/2 electronic systems on the experimental observation of novel higher-order band touchings because the system does

not have to be finely tuned to preserve certain symmetry, for example, the equal SO coupling strengths M_{0x} and M_{0y} for C_4 symmetry.

VI. CONCLUSION

In summary, we studied the physics and experimental realization of pseudospin-1 Fermi gases with 2D Rashba-type SO coupling and found many exotic topological quantum phases, such as triply degenerate points, quadratic and cubic band touchings, triple-Weyl nodes, and so on. Our work provides an alternative route for engineering many fascinating topological quantum matters by utilizing large spin degrees, instead of complex optical lattice geometry (see Appendix F for a discussion of robustness against lattice distortions). Our results may motivate further theoretical and experimental investigations of interesting SO coupling effects in larger spin systems.

APPENDIX A: SPIN-1 PAULI MATRICES

The spin vectors are usually defined as the finite-dimensional irreducible representation of SU(2) which has a dimension $2s + 1$ for spin-s systems. By convention, we denote the spin-1/2 spin operator as $S_{1/2} = \frac{\hbar}{2}\sigma$, where $\sigma = (\sigma_x, \sigma_y, \sigma_z)$ denotes the Pauli matrices. Similarly, for a spin-1 system we have $S_1 = \frac{\hbar}{2}F$, where

$$
F_x = \begin{pmatrix} 0 & \sqrt{2} & 0 \\ \sqrt{2} & 0 & \sqrt{2} \\ 0 & \sqrt{2} & 0 \end{pmatrix}, \quad F_y = \begin{pmatrix} 0 & -\sqrt{2}i & 0 \\ \sqrt{2}i & 0 & -\sqrt{2}i \\ 0 & \sqrt{2}i & 0 \end{pmatrix},
$$
(A1)

and $F_z = \mathrm{diag}(-2, 0, 2)$ is diagonal.

Note that, F_z and F_z^2 form the Cartan subalgebra of SU(3) and thus, any in-plane Zeeman field can be linearly decomposed up to a constant.

APPENDIX B: SINGLE-PARTICLE PHASE DIAGRAM

By tuning the detunings $\delta_{\pm 1}$, we can change the relative energy between different bands. For a very large $\delta_{\pm 1}$, either the top or bottom band is pulled far away and the spin-1 model can be reduced to a spin-1/2 system, which was studied by the authors of Ref. [51]. With such an observation we expect to observe interesting topological phases in the spin-1 model when one of the detunings satisfies $0 < |\delta_{\pm 1}| < 8t$. In Figs. 5(a) and 5(b), the phase diagrams of the Chern number for two upper bands are plotted with respect to $\delta_{\pm 1}$. Note that the phase diagram for the lowest band was presented in the main text.

Since the upper and lower bands are only coupled to the middle band, similarly to the spin-1/2 case, they should have $C = \pm 1$ when $0 < |\delta_{\pm 1}| < 8t$. If the Chern numbers of those two bands have opposite sign, the middle band must be trivial. Otherwise, the middle band has a large Chern number $C = \pm 2$ in the opposite way, as illustrated in Fig. 5(c). Such a combination makes the phase diagram of the middle band much richer. If we consider only the topological phase transition points from the spin-1/2 case, i.e., $\delta_{\pm 1} = 0, \pm 8t$, the $(\delta_{+1}, \delta_{-1})$ plane is divided in to 16 square (rectangle) regions with different Chern number $\pm 2, \pm 1$, and 0. In most cases, the transition is characterized by the emergence of Dirac cones at high-symmetry points in BZ. An interesting example in which the middle band touches both the lower and upper bands is shown in Fig. 5(d).

Each Dirac cone carries a Berry flux $\pm \pi$, which changes the Chern number by ± 1. In this sense, when the Chern number is changed by ± 2 (± 2 to 0 or ± 1 to ∓ 1), a pair of Dirac cones must appear. Note that, unlike a spin-1/2 system, the Dirac cone here is not protected by the time-reversal symmetry, although its low-energy Hamiltonian does exhibit such a symmetry. For the phase transition from Chern number ± 2 to ∓ 2, a possible mechanism is that four Dirac cones appear with each one contributing a change of 1. However, this is not the case here. In our model, four high-symmetry
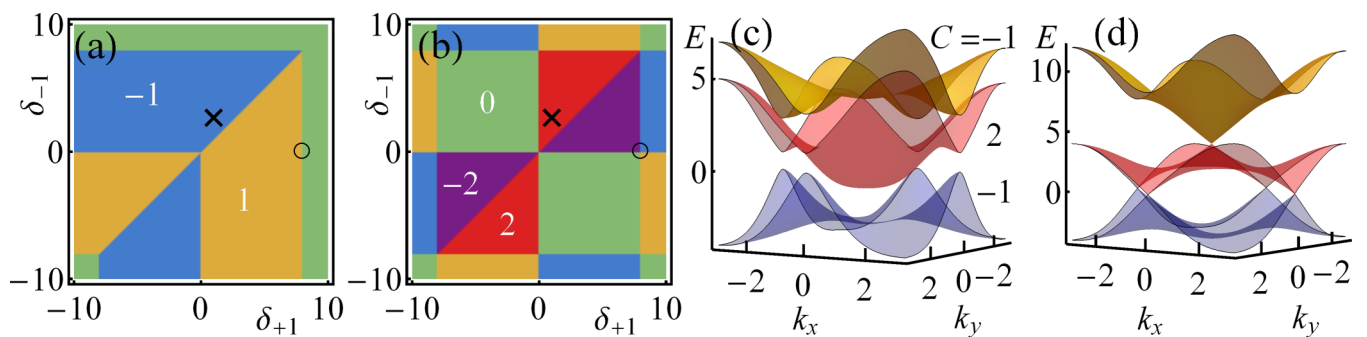

FIG. 5. (a, b) The Chern number for upper and middle bands in the plane $(\delta_{+1}, \delta_{-1})$, respectively. The summation over the Chern number of all three bands equals to 0. (c) A typical band structure when all bands are well separated and the middle band has a Chern number of 2. The Zeeman fields are chosen as the dark cross in panel (a, b). (d) The single Dirac band touching between adjacent bands at high-symmetry points in BZ. The parameters are labeled by the dark circle in (b). The circle locates on multiple boundaries, where the middle band crosses with both lower and upper bands.

points fall into two groups, which are mutually exclusive for weak Zeeman fields. Therefore we cannot expect to have four of the same type of band touching points between two bands, and higher-order band touching points with quantized nonzero (and $> \pi$) Berry flux must appear to have a large change (± 4) of the Chern number. Such quadratic band touching and associated band structure were studied explicitly in the main text.

Similarly, with increasing δ_T, the lower band is pulled away from the triply degenerate point and the upper two bands are degenerate with quadratic band dispersion. However, the band Chern number vanishes after the gapless points are open because the upper two bands have quadratic band touchings at all Γ, M, and two X points with wind number -2, -2, and $2 * 2$, whose summation is zero.

APPENDIX C: (TRIPLE-)WEYL POINTS AND EDGE STATES

In Fig. 6(a), the triple-Weyl point shown in Fig. 3(b) is also plotted in the k_z'-k_x plane (the right touching point), which shows a linear band dispersion along k_z'. The band touching on the left is a Weyl point, indicated by the red disks in Figs. 3(a) and 3(c). Another Weyl point at larger $|k_z|$ [the yellow triangles in Figs. 3(a) and 3(c)] appears at the M point $k_x = k_y = \pi$ as shown in Fig. 6(b).

The corresponding edge states for a few 2D band structures with fixed k_z' are shown in Figs. 6(c) to 6(e). When k_z' lies in between two Γ Weyl points, there are three edge modes Fig. 6(c), agreeing with the bulk Chern number 3 [Fig. 3(a)]. However, one of these edge modes crosses zero energy twice, leading to four surface arcs observed in Fig. 3(c) and large surface-state density at $k_y = 0$. Across the Γ Weyl point, the

band gap at $k_y = 0$ for the twisted edge state is opened, and the number of edge states becomes four, agreeing with the bulk Chern number of 4 in Fig. 3(a). When k_z' further increases and we cross the Γ tripe-Weyl node, only one edge state at $k_y = \pi$ is left as shown in Fig. 6(e), agreeing with the bulk Chern number of 1.

APPENDIX D: EFFECTIVE HAMILTONIAN AND TIGHT-BINDING MODEL

As illustrated in Fig. 4(a), two beams (red lines) are incident from both the x and z directions and reflected by two mirrors to form two standing waves $\boldsymbol{E}_{1x} = \hat{z}E_{1x}e^{i(\varphi_{1x}+\varphi_{1z}+\varphi_L)/2}\cos(k_0 x + \alpha)$ and $\boldsymbol{E}_{1z} = \hat{x}E_{1z}e^{i(\varphi_{1x}+\varphi_{1z}+\varphi_L)/2}\cos(k_0 z + \beta)$, where $E_{1x(z)}$ is the field strength, $\varphi_{1x(z)}$ is the initial phase, $\varphi_L = k_0 K$ is the phase picked up from optical path K, and $\alpha(\beta) = (\varphi_{1x(z)} - \varphi_{1z(x)} - \varphi_L)/2$. Another two beams (blue and green lines) are incident along the z direction to form plane-waves $\boldsymbol{E}_{2(3)z} = \hat{x}E_{2(3)z}e^{i(k_0 z + \varphi_{2(3)})}$ and $\boldsymbol{E}_{2(3)x} = \hat{z}E_{2(3)x}e^{i(-k_0 x + \varphi_{2(3)} + \varphi_L - \delta\varphi_{2(3)})}$ with the initial phases $\varphi_{2(3)}$ and relative phases $\delta\varphi_{L2(3)} = (\omega_1 - \omega_{2(3)})K/c$.

The level diagram and optical couplings are illustrated in Fig. 4(b). Although both transition lines $D_2({}^2S_{1/2} \to {}^2P_{3/2})$ and $D_1({}^2S_{1/2} \to {}^2P_{1/2})$ contribute to the coupling, the second is negligible due to large detuning Δ. As a result, we mainly consider the contribution from D_2 transitions. The optical dipole potentials are summed over all possible transitions

$$V_{m_\sigma,T}(x) = \frac{|\Omega_{1x,m_\sigma,T}|^2}{\Delta_p}, \quad V_{m_\sigma,T}(z) = \frac{|\Omega_{1z,m_\sigma,T}|^2}{\Delta_p}, \quad \text{(D1)}$$

where $m_\sigma = +9/2, +7/2, +5/2$ denotes the value of m_F for each spin component (corresponding to $+1$, 0, and -1,
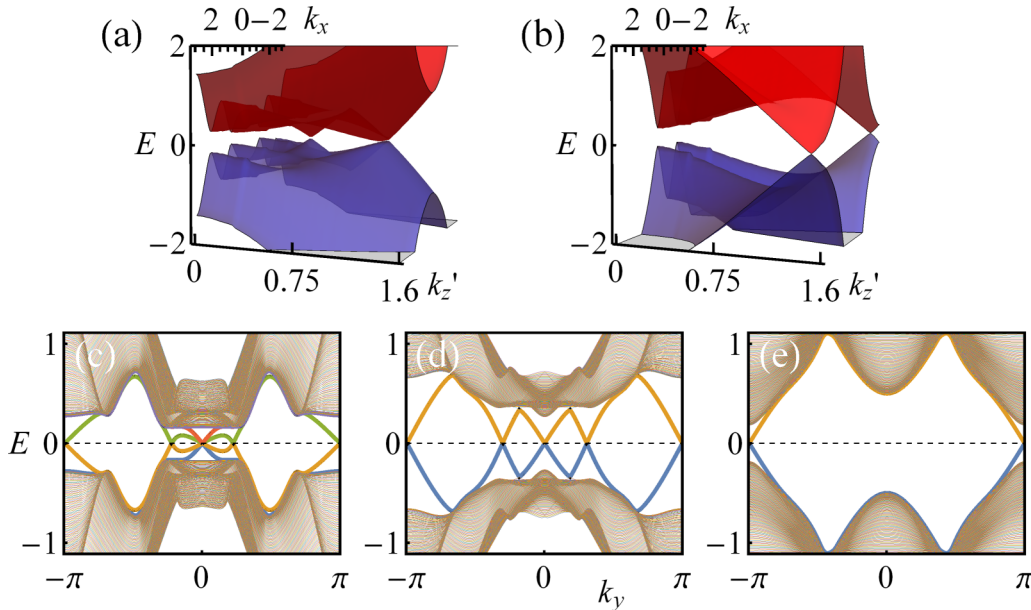

FIG. 6. (a) Band structure in the $k_y = 0$ plane. The triple-Weyl node locates on the right side and the dispersion is linear along the k_z' direction. On the left-hand side, there is a Weyl point with linear dispersions along all directions. (b) Band structure in the $k_y = \pi$ plane with a M Weyl point. (c–e) Edge states along k_y with fixed $k_z' = 0.45$, $k_z = 0.77'$, and $k_z' = 1.45$, respectively. The other parameters are the same as those in Fig. 3.

respectively) and $T = \sigma^\pm, \pi$ represents three different transitions. The effective Rabi frequency $\Omega_{1x(z),m_\sigma,T}$ is defined through

$$\Omega_{1x,m_\sigma,T} = \sqrt{\sum_F |\Omega_{x,F,m_\sigma,T}|^2},$$

$$\Omega_{1y,m_\sigma,T} = \sqrt{\sum_F |\Omega_{z,F,m_\sigma,T}|^2}, \quad F = \frac{11}{2}, \frac{9}{2}, \ldots, m_\sigma,$$

$$\text{(D2)}$$

with

$$|\Omega_{x(z),F,m_\sigma,\sigma^+}| = |\mu_{m_\sigma,F,\sigma^+}||E_{1x(z)}|,$$
$$|\mu_{m_\sigma,F,\sigma^+}| = \left\langle \frac{9}{2}, m_\sigma | \boldsymbol{r} \cdot \epsilon_{1x(z)} | F, m_\sigma + 1 \right\rangle,$$
$$|\Omega_{x(z),F,m_\sigma,\pi}| = |\mu_{m_\sigma,F,\pi}||E_{1x(z)}|,$$
$$|\mu_{m_\sigma,F,\pi}| = \left\langle \frac{9}{2}, m_\sigma | \boldsymbol{r} \cdot \epsilon_{1x(z)} | F, m_\sigma \right\rangle,$$
$$|\Omega_{x(z),F,m_\sigma,\sigma^-}| = |\mu_{m_\sigma,F,\sigma^-}||E_{1x(z)}|,$$
$$|\mu_{m_\sigma,F,\sigma^-}| = \left\langle \frac{9}{2}, m_\sigma | \boldsymbol{r} \cdot \epsilon_{1x(z)} | F, m_\sigma - 1 \right\rangle,$$

where $\epsilon_{1x(z)}$ are the polarization vectors of lasers. For a π transition, we have

$$V_{+1,\pi,x(z)} : V_{0,\pi,x(z)} : V_{-1,\pi,x(z)}$$
$$= \sum_F |\mu_{9/2,F,\pi}|^2 : \sum_F |\mu_{7/2,F,\pi}|^2 : \sum_F |\mu_{5/2,F,\pi}|^2, \quad \text{(D3)}$$

which is

$$V_{+1,\pi,x(z)} : V_{0,\pi,x(z)} : V_{-1,\pi,x(z)}$$
$$= 1215 + 3240 : 2187 + 1960 + 308 : 2916 + 1000$$
$$+ 539$$
$$= 1 : 1 : 1$$

for the experimental data of ^{40}K. Similarly, we can calculate those coefficients for $\sigma^\pm$ transitions

$$V_{+1,\sigma^\pm,x(z)} : V_{0,\sigma^\pm,x(z)} : V_{-1,\sigma^\pm,x(z)}$$
$$= 13365 + 243 + 1440 + 2772 : 10935 + 1440 + 729$$
$$+ 2560 + 2156 : 8748 + 2560 + 77 + 1458$$
$$+ 3360 + 1617$$
$$= 1 : 1 : 1.$$

One can also verify that this still holds true even when we take the D_1 line into account. Therefore this lattice potential is indeed spin-independent and can be written as

$$V(\boldsymbol{r}) = V(x) + V(z)$$
$$= V_{0x} \cos^2(k_0 x + \alpha) + V_{0z} \cos^2(k_0 z + \beta). \quad \text{(D4)}$$

As shown in Fig. 4(b), each plane-wave induces two Raman couplings. The four coupling strengths are

$$M_{1x,2z} = \sum_F \frac{\Omega^*_{1x,F,9/2}\Omega_{2z,F,7/2}}{\Delta_p},$$

$$M_{1z,2x} = \sum_F \frac{\Omega^*_{1z,F,9/2}\Omega_{2x,F,7/2}}{\Delta_p},$$

$$M_{1x,3z} = \sum_F \frac{\Omega^*_{1x,F,7/2}\Omega_{3z,F,5/2}}{\Delta_p},$$

$$M_{1z,3x} = \sum_F \frac{\Omega^*_{1z,F,7/2}\Omega_{3x,F,5/2}}{\Delta_p},$$

where

$$\Omega_{ix,F,\sigma_m} = \left\langle \frac{9}{2}, m_\sigma | \hat{x} \cdot \epsilon_{ix} | F, m_\sigma \right\rangle E_{ix}, i = 1, 2, 3;$$
$$\Omega_{1z,F,\sigma_m} = \left\langle \frac{9}{2}, m_\sigma | \hat{z} \cdot \epsilon_{1z} | F, m_\sigma - 1 \right\rangle E_{1z},$$
$$\Omega_{iz,F,\sigma_m} = \left\langle \frac{9}{2}, m_\sigma | \hat{z} \cdot \epsilon_{iz} | F, m_\sigma + 1 \right\rangle E_{iz}, i = 2, 3.$$

After inserting the effective Rabi frequency, we obtain

$$M_{2(3)z,1x} = M_{0,2(3)x}$$
$$\times \cos(k_0 x + \alpha)e^{-i(k_0 z + \beta)}e^{i(\varphi_{2(3)} - \varphi_{1z})},$$
$$M_{2(3)x,1z} = M_{0,2(3)z}$$
$$\times \cos(k_0 z + \beta)e^{i(k_0 x + \alpha)}e^{i(\delta\varphi_{L2(3)} + \varphi_{2(3)} - \varphi_{1z})}.$$

Note that the terms proportional to $\cos(k_0 x)\cos(k_0 z)$ are antisymmetric to each lattice site in both the x and z directions and thus can be neglected for low-band physics [51]. The resulting coupling strengths are

$$\mathcal{M}_{2(3)x} = -M_{2(3)x} + M_{2(3)y}\cos\delta\varphi_{L2(3)}, \quad \text{(D5)}$$

$$\mathcal{M}_{2(3)y} = M_{2(3)y}\sin\delta\varphi_{L2(3)}, \quad \text{(D6)}$$

with $M_{2(3)x} = M_{0,2(3)x}\cos(k_0 x + \alpha)\sin(k_0 z + \beta)$ and $M_{2(3)y} = M_{0,2(3)y}\cos(k_0 z + \beta)\sin(k_0 x + \alpha)$. In the following, we assume that the strengths of the incident beams are tuned such that $\mathcal{M}_{2x(y)} = \mathcal{M}_{3x(y)} = \mathcal{M}_{x(y)}$. Now, the total effective Hamiltonian in two dimensions can be written as

$$H = \frac{\boldsymbol{p}^2}{2m} + V(\boldsymbol{r}) + \mathcal{M}_x F_x + \mathcal{M}_y F_y + \delta_T F_z^2 + \delta_V F_z. \quad \text{(D7)}$$

If $\delta\varphi_L = n\pi, n \in \mathbb{Z}$, the SO coupling becomes 1D. Here, we set $\delta\varphi_L = \pi/2$ and $\alpha, \beta = 2n\pi$ such that the coupling terms become

$$M_x(x, z) = -M_{0x}\cos(k_0 x)\sin(k_0 z), \quad \text{(D8)}$$

$$M_y(x, z) = -M_{0y}\cos(k_0 z)\sin(k_0 x). \quad \text{(D9)}$$

As we only consider the lowest s orbital $\phi_{s,\sigma}$ ($\sigma = +1, 0, -1$) and nearest-neighbor hopping, the tight-binding Hamiltonian is

$$H_{\text{TI}} = - \sum_{\langle \boldsymbol{i},\boldsymbol{j}\rangle,\sigma} t^{ij}\hat{c}^\dagger_{i,\sigma}\hat{c}_{j,\sigma}$$
$$+ \sum_{\langle \boldsymbol{i},\boldsymbol{j}\rangle}\left(t^{ij}_{\text{so},+}\hat{c}^\dagger_{i,+1}\hat{c}_{j,0} + \text{H.c.} + t^{ij}_{\text{so},-}\hat{c}^\dagger_{i,0}\hat{c}_{j,-1} + \text{H.c.}\right)$$
$$+ \delta_T \sum_i (\hat{n}_{i,+1} + \hat{n}_{i,-1}) + \delta_V \sum_i (\hat{n}_{i,+1} - \hat{n}_{i,-1}),$$
$$\text{(D10)}$$

where hopping strengths can be expressed as overlap integrals

$$t^{ij} = \int d^2\boldsymbol{r}\phi^i_{s,\sigma}(\boldsymbol{r})\left[\frac{\boldsymbol{p}^2}{2m} + V(\boldsymbol{r})\right]\phi^i_{s,\sigma}(\boldsymbol{r}), \quad \text{(D11)}$$

and

$$t_{so,+}^{ij} = \int d^2\boldsymbol{r}\phi_{s,+1}^i(\boldsymbol{r})[M_x(x,z)F_x + M_y(x,z)F_y]\phi_{s,0}^i(\boldsymbol{r}),$$

$$t_{so,-}^{ij} = \int d^2\boldsymbol{r}\phi_{s,0}^i(\boldsymbol{r})[M_x(x,z)F_x + M_y(x,z)F_y]\phi_{s,-1}^i(\boldsymbol{r}).$$

While the usual nearest-neighbor hopping is obviously the same at different sites in all directions, the spin-flip process is more subtle. Even though it has been generalized to the spin-1 system, the reasoning of the authors of Ref. [10] is still valid and thus the Raman potential hopping is staggered as

$$t_{so}^{i_x,i_x\pm 1} = \pm(-1)^{i_x+i_z}t_{so}, t_{so}^{i_z,i_z\pm 1} = \pm i(-1)^{i_x+i_z}t_{so}. \quad \text{(D12)}$$

Upon applying the transformations $\hat{c}_{i,0} \to e^{i\pi(x_i+z_i)}\hat{c}_{i,0}$ and $\hat{c}_{i,-1} \to e^{i2\pi(x_i+z_i)}\hat{c}_{i,-1}$ and a Fourier transformation, we obtain our model Hamiltonian in momentum-space up to some constants (where we also defined the lattice constant $a = \frac{\pi}{k_0}$ as the unit of length). We remark that such a unitary transformation does not affect the form of interatomic interaction.

APPENDIX E: EXTENSION TO LARGER SPINS

In the last subsection in the main text, we generalize our results on high-order band touching to a genuine large spin system and compare them to those in electronic systems enriched by special point-group symmetry C_n. This Appendix provides some detailed discussions.

Considering a spin-s system, our model Eq. (1) can be extended to $H_0 = -\sum_{\boldsymbol{k},l\neq j} h_{\boldsymbol{k},l,j}\hat{c}_{\boldsymbol{k},l}^\dagger\hat{c}_{\boldsymbol{k},j}$ where the spin indices $-s \leqslant l,j \leqslant s$ enumerate each spin component. The matrix element of $h_{\boldsymbol{k},l,j}$ can be written as $h_{l,l} = \delta_l + t_l[\cos(k_x) + \cos(k_y)]$, $h_{l,l+1} = t_{l,l+1,y}\sin(k_y) + it_{l,l+1,x}\sin(k_x)$, and $h_{l,l+1} = h_{l+1,l}^*$. In the following, we drop the subscript $\boldsymbol{k}$ for convenience and assume all coupling constants are real. The coupling terms $t_{l,l+1,x}$ and $t_{l,l+1,y}$ are generic since we imposed no special symmetry. A band touching point appears at the two X (Γ and M) points for $\delta_l = \delta_j$ ($\delta_l + 2t_l = \delta_j + 2t_j$ and $\delta_l - 2t_l = \delta_j - 2t_j$). In our previous discussion, $t_l = t_j$, therefore the band touchings at Γ and M always accompany each other.

We start from the case where degeneracy only happens between two spin components l and j ($j > l$). Expanding the Hamiltonian around a band touching point at one of the four high-symmetry points $\boldsymbol{K_n}$, one has the following two-level effective Hamiltonian:

$$H(\boldsymbol{K_n} + \boldsymbol{q}) = g(\boldsymbol{q})\sigma_+ + g^*(\boldsymbol{q})\sigma_- + \delta\sigma_z, \quad \text{(E1)}$$

where $\sigma_\pm = \sigma_x \pm i\sigma_y$ and $q = |\boldsymbol{q}|$ is assumed to be small. Any other diagonal term is neglected and δ is introduced for later convenience. So far we discuss $\delta = 0$ for the single-particle case. The coupling term would be in the form $g(\boldsymbol{q}) = \Pi_{l\leqslant k<j}(a_kqe^{i\theta_k} - b_k)$ in general and the constants b_k come from expanding the trigonometric function around $\boldsymbol{K_n}$. Notice that this gives, up to some constants, the Cartesian products of three real irreducible representations of point group C_n, therefore it is not surprising to see the low-energy Hamiltonian of the high-order band touching point in our model shares the same form as those stabilized by C_n rotational symmetry [32,41]. When $a_k \neq 0$ and each θ_k can be well defined, this high-order band touching point has a

multiplicity $m = j - l$. Note that, generally, this multiplicity is not equal to the Berry flux of such a crossing point. In fact, the winding number of this touching point is $\sum_k \text{sign}(\theta_k)$. If $\text{sign}(\theta_k)$ can be tuned (i.e., the relative sign between $t_{k,k+1,x}$ and $t_{k,k+1,y}$), we are able to engineer a m-order band touching point with possible Berry flux $m\pi$, $(m-2)\pi$,..., $(-m+2)\pi$, $-m\pi$. For example, for the coupling $k_xF_y + k_yF_x$ and in the region $\text{sign}(\delta_{+1})\text{sign}(\delta_{-1}) > 0$ and $-8 < \delta_{\pm 1} < 8$, we have a large Chern number phase with the phase transition characterized by quadratic band touching carrying a -2π Berry flux. However, if the model is modified to $k_yF_x \pm k_x\{F_y, F_z\}$ (time-reversal symmetry has been broken), the band touching point still shows a quadratic dispersion, but becomes topologically trivial.

Now, assume we have multiple degeneracy among spin components $-s \leqslant s_1 < s_2 < \cdots < s_n \leqslant s$ when $\delta_{s_k} = \delta_{c,s_k}$, $s_k \in S = \{s_1, s_2, \ldots, s_n\}$ at a certain $\boldsymbol{K_n}$ in BZ. The whole phase diagram for a given band would have dimension $2s$. We first consider one ordered pair s_i and s_j with $s_j > s_i$, $s_i, s_j \in S$. Following what we discussed above, this defines a gapless ($2s - 1$-dimensional) subspace R_{s_i,s_j} with a $s_j - s_i$ order band touching point carrying some winding number w_{s_i,s_j} if δ_{s_k} is slightly deviated from δ_{c,s_k} for any $s_k \in S$ and $s_k \neq s_i, s_j$. The multiply degenerate point exists in the subspace expressed as $\cup_{(s_i,s_j)}R_{(s_i,s_j)}$ when δ_{s_k} approaches δ_{c,s_k} from all allowed directions and has a winding number w_{s_0,s_n}, which is equal to $\sum_{1\leqslant i<n} w_{s_i,s_{(i+1)}}$. Thus, one would obtain a topologically nontrivial multiply degenerate point as a generalization of triply degenerate point in a lager spin system.

So far we have seen that the high-order band touching point conceived in our system can be ascribed to degeneracy and indirect coupling between degenerate spin components. Thus, it would be natural to have even higher-order band crossing when pairing is introduced. The pairing order parameter $\Delta_{i,j}$ between spin component i and j enters the BdG Hamiltonian as complex numbers and opens superconducting gaps. We would consequently see many gapped topological superfluids with large Chern numbers and high-order band touching points that serve as topological phase transition points. However, $\Delta_{i,j}$ is a constant and contributes neither multiplicity nor winding to a band touching point. In previous discussions, we only consider pairing between $|0\rangle$ and $|1\rangle$ to have a cubic band touching.

When the third spatial dimension is included, it appears in the diagonal terms as free single-particle kinetic energy. After expanding the system Hamiltonian around a band touching at $\boldsymbol{K_n}$ and some k'_{z0} we have $\delta = k'_z$ in Eq. (E1). Now, Eq. (E1) is a direct generalization of chiral Weyl fermions in free space. Such a multi-Weyl node may carry a large charge and is spatially anisotropic, i.e., it is linear along k_z but shows high-order dispersion along k_x and k_y. We expect exotic chiral magnetic effects due to the nonlinear band structure of multi-Weyl nodes, as compared to traditionally defined Weyl fermions [44].

APPENDIX F: ROBUSTNESS OF BAND TOUCHING AGAINST DISTORTED LATTICE

In the main text, we consider the SO-coupled Fermi gases on a regular square lattice with C_4 symmetry. While we
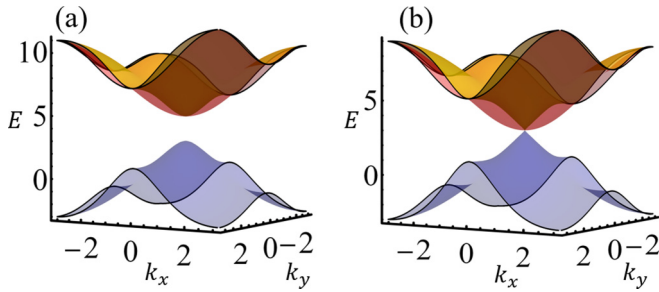
FIG. 7. (a) Similar to Fig. 1(a) but plotted with symmetry breaking terms such that $t_x = 1$, $t_y = 0.5$, $t_{SO,x} = 1$, and $t_{SO,y} = 0.5$. (b) With such an anisotropy, the 2D triply degenerate point now occurs at $\delta_T = 6$.

provided physical insights into the symmetry protection using the coupling scheme depicted in Fig. 1(c), we offer a numerical verification in this Appendix.

To show that the rotational symmetry does not affect the band touchings studied in Sec. II, here we distort lattice potential to be anisotropic. Consequently, both the bare hopping and SO coupling along x and y are no longer the same. We compare in Figs. 1(a) and 7(a) how such an anisotropy affects the single-particle band structures. The quadratic band touchings at the corners and the sides of the Brillouin zone survive while it seems apparently that the 2D triply degenerate point vanishes. In fact, the triply degenerate point is merely shifted along the time-reversal symmetry line in parameter space and is now located at $\delta_T = 6$.

[1] Y.-J. Lin, K. Jiménez-García, and I. B. Spielman, Spin-orbit-coupled Bose-Einstein condensates, Nature **471**, 83 (2011).

[2] J.-Y. Zhang *et al.*, Collective Dipole Oscillations of a Spin-Orbit Coupled Bose-Einstein Condensate, Phys. Rev. Lett. **109**, 115301 (2012).

[3] P. Wang, Z. Q. Yu, Z. Fu, J. Miao, L. Huang, S. Chai, H. Zhai, and J. Zhang, Spin-Orbit Coupled Degenerate Fermi Gases, Phys. Rev. Lett. **109**, 095301 (2012).

[4] L. W. Cheuk, A. T. Sommer, Z. Hadzibabic, T. Yefsah, W. S. Bakr, and M. W. Zwierlein, Spin-Injection Spectroscopy of a Spin-Orbit Coupled Fermi Gas, Phys. Rev. Lett. **109**, 095302 (2012).

[5] R. A. Williams, M. C. Beeler, L. J. LeBlanc, K. Jiménez-García, and I. B. Spielman, Raman-Induced Interactions in a Single-Component Fermi Gas Near an *S*-Wave Feshbach Resonance, Phys. Rev. Lett. **111**, 095301 (2013).

[6] C. Qu, C. Hamner, M. Gong, C. Zhang, and P. Engels, Observation of Zitterbewegung in a spin-orbit coupled Bose-Einstein condensate, Phys. Rev. A **88**, 021604(R) (2013).

[7] A. J. Olson, S.-J. Wang, R. J. Niffenegger, C.-H. Li, C. H. Greene, and Y. P. Chen, Tunable Laudan-Zener transitions in a spin-orbit-coupled Bose-Einstein condensate, Phys. Rev. A **90**, 013616 (2014).

[8] L. H. Huang *et al.*, Experimental realization of two-dimensional synthetic spin-orbit coupling in ultracold Fermi gases, Nat. Phys. **12**, 540 (2016).

[9] Z. Meng, L. Huang, P. Peng, D. Li, L. Chen, Y. Xu, C. Zhang, P. Wang, and J. Zhang, Experimental Observation of a Topological Band Gap Opening in Ultracold Fermi Gases with Two-Dimensional Spin-Orbit Coupling, Phys. Rev. Lett. **117**, 235304 (2016).

[10] Z. Wu *et al.*, Realization of two-dimensional spin-orbit coupling for Bose-Einstein condensates, Science **354**, 83 (2016).

[11] W. Sun *et al.*, Highly Controllable and Robust 2D Spin-Orbit Coupling for Quantum Gases, Phys. Rev. Lett. **121**, 150401 (2018).

[12] A. Valdés-Curiel, D. Trypogeorgos, Q.-Y. Liang, R. P. Anderson, and I. B. Spielman, *Unconventional topology with a Rashba spin-orbit coupled quantum gas*, arXiv:1907.08637.

[13] D. L. Campbell, R. M. Price, A. Putra, A. Valdé s-Curiel, D. Trypogeorgos, and I. B. Spielman, Magnetic phases of spin-1 spin–orbit-coupled Bose gases, Nat. Commun. **7**, 10897 (2016).

[14] X. Luo, L. Wu, J. Chen, Q. Guan, K. Gao, Z.-F. Xu, L. You, and R. Wang, Tunable atomic spin-orbit coupling synthesized with a modulating gradient magnetic field, Sci. Rep. **6**, 18983 (2016).

[15] Z. Lan and P. Öhberg, Raman-dressed spin-1 spin-orbit-coupled quantum gas, Phys. Rev. A **89**, 023630 (2014).

[16] S. S. Natu, X. Li, and W. S. Cole, Striped ferronematic ground states in a spin-orbit-coupled S=1 Bose gas, Phys. Rev. A **91**, 023608 (2015).

[17] K. Sun, C. Qu, Y. Xu, Y. Zhang, and C. Zhang, Interacting spin-orbit-coupled spin-1 Bose-Einstein condensates, Phys. Rev. A **93**, 023615 (2016).

[18] Z.-Q. Yu, Phase transitions and elementary excitations in spin-1 Bose gases with Raman-induced spin-orbit coupling, Phys. Rev. A **93**, 033648 (2016).

[19] G. I. Martone, F. V. Pepe, P. Facchi, S. Pascazio, and S. Stringari, Tricriticalities and Quantum Phases in Spin-Orbit-Coupled Spin-1 Bose Gases, Phys. Rev. Lett. **117**, 125301 (2016).

[20] E. J. König and J. H. Pixley, Quantum Field Theory of Nematic Transitions in Spin-Orbit-Coupled Spin-1 Polar Bosons, Phys. Rev. Lett. **121**, 083402 (2018).

[21] B. Bradlyn *et al.*, Beyond Dirac and Weyl fermions: Unconventional quasiparticles in conventional crystals, Science **353**, aaf5037 (2016).

[22] G. W. Winkler, Q.-S. Wu, M. Troyer, P. Krogstrup, and A. A. Soluyanov, Topological Phases in InAs$_{1-x}$Sb$_x$: From Novel Topological Semimetal to Majorana Wire, Phys. Rev. Lett. **117**, 076403 (2016).

[23] H. M. Weng, C. Fang, Z. Fang, and X. Dai, Topological semimetals with triply degenerate nodal points in θ-phase tantalum nitride, Phys. Rev. B **93**, 241202(R) (2016).

[24] Z. M. Zhu, G. W. Winkler, Q. S. Wu, J. Li, and A. A. Soluyanov, Triple Point Topological Metals, Phys. Rev. X **6**, 031003 (2016).

[25] H. M. Weng, C. Fang, Z. Fang, and X. Dai, Coexistence of Weyl fermion and massless triply degenerate nodal points, Phys. Rev. B **94**, 165201 (2016).

[26] B. Q. Lv *et al.*, Observation of three-component fermions in the topological semimetal molybdenum phosphide, Nature **546**, 627 (2017).

[27] J.-Z. Ma *et al.*, Three-component fermions with surface Fermi arcs in tungsten carbide, Nat. Phys. **14**, 349 (2018).

[28] H. Hu, J. Hou, F. Zhang, and C. Zhang, Topological Triply Degenerate Points Induced by Spin-Tensor-Momentum Couplings, Phys. Rev. Lett. **120**, 240401 (2018).

[29] J. Hou, Z. Li, X.-W. Luo, Q. Gu, and C. Zhang, Topological Bands and Triply-Degenerate Points in Non-Hermitian Hyperbolic Metamaterials, Phys. Rev. Lett. **124**, 073603 (2020).

[30] D. Xiao, W. Yao, and Q. Niu, Valley Contrasting Physics in Graphene: Magnetic Moment and Topological Transport, Phys. Rev. Lett. **99**, 236809 (2007).

[31] K. Sun and E. Fradkin, Time-reversal symmetry breaking and spontaneous anomalous Hall effect in Fermi fluids, Phys. Rev. B **78**, 245122 (2008).

[32] K. Sun, H. Yao, E. Fradkin, and S. A. Kivelson, Topological Insulators and Nematic Phases from Spontaneous Symmetry Breaking in 2D Fermi Systems with a Quadratic Band Crossing, Phys. Rev. Lett. **103**, 046811 (2009).

[33] I. F. Herbut and L. Janssen, Topological Mott Insulator in Three-Dimensional Systems with Quadratic Band Touching, Phys. Rev. Lett. **113**, 106401 (2014).

[34] S. Pujari, T. C. Lang, G. Murthy, and R. K. Kaul, Interaction-Induced Dirac Fermions from Quadratic Band Touching in Bilayer Graphene, Phys. Rev. Lett. **117**, 086404 (2016).

[35] H.-Q. Wu, Y.-Y. He, C. Fang, Z. Y. Meng, and Z.-Y. Lu, Diagnosis of Interaction-driven Topological Phase via Exact Diagonalization, Phys. Rev. Lett. **117**, 066403 (2016).

[36] W. Zhu, S.-S. Gong, T.-S. Zeng, L. Fu, and D. N. Sheng, Interaction-Driven Spontaneous Quantum Hall Effect on a Kagome Lattice, Phys. Rev. Lett. **117**, 096402 (2016).

[37] M. Chen, H.-Y. Hui, S. Tewari, and V. W. Scarola, Quantum anomalous Hall state from spatially decaying interactions on the decorated honeycomb lattice, Phys. Rev. B **97**, 035114 (2018).

[38] F. Wilczek, Majorana returns, Nat. Phys. **5**, 614 (2009).

[39] J. Alicea, New directions in the pursuit of Majorana fermions in solid state systems, Rep. Prog. Phys. **75**, 076501 (2012).

[40] M. Franz, Majorana's wires, Nat. Nano **8**, 149 (2013).

[41] C. Fang, M. J. Gilbert, X. Dai, and B. A. Bernevig, Multi-Weyl Topological Semimetals Stabilized by Point Group Symmetry, Phys. Rev. Lett. **108**, 266802 (2012).

[42] S.-M. Huang *et al.*, New type of Weyl semimetal with quadratic double Weyl fermions, Proc. Natl. Acad. Sci. USA **113**, 1180 (2016).

[43] S.-X. Zhang, S.-K. Jian, and H. Yao, Correlated triple-Weyl semimetals with Coulomb interactions, Phys. Rev. B **96**, 241111(R) (2017).

[44] Z.-M. Huang, J. Zhou, and S.-Q. Shen, Topological responses from chiral anomaly in multi-Weyl semimetals, Phys. Rev. B **96**, 085201 (2017).

[45] Q. Liu and A. Zunger, Predicted Realization of Cubic Dirac Fermion in Quasi-One-Dimensional Transition-Metal Monochalcogenides, Phys. Rev. X **7**, 021019 (2017).

[46] X.-Y. Mai, D.-W. Zhang, Z. Li, and S.-L. Zhu, Exploring topological double-Weyl semimetals with cold atoms in optical lattices, Phys. Rev. A **95**, 063616 (2017).

[47] C. Chin, R. Grimm, P. Julienne, and E. Tiesinga, Feshbach resonances in ultracold gases, Rev. Mod. Phys. **82**, 1225 (2010).

[48] Z. Fu *et al.*, Production of Feshbach molecules induced by spin–orbit coupling in Fermi gases, Nat. Phys. **10**, 110 (2014).

[49] C. Qu, Z. Zheng, M. Gong, Y. Xu, L. Mao, X. Zou, G. Guo, and C. Zhang, Topological Superfluids with Finite Momentum Pairing and Majorana Fermions, Nat. Commun. **4**, 2710 (2013).

[50] Y. Xu, F. Zhang, and C. Zhang, Structured Weyl Points in Spin-Orbit Coupled Fermionic Superfluids, Phys. Rev. Lett. **115**, 265304 (2015).

[51] X.-J. Liu, K. T. Law, and T. K. Ng, Realization of 2D Spin-Orbit Interaction and Exotic Topological Orders in Cold Atoms, Phys. Rev. Lett. **112**, 086401 (2014).

[52] B. Song, L. Zhang, C. He, T. F. J. Poon, E. Hajiyev, S. Zhang, X.-J. Liu, and G.-B. Jo, Observation of symmetry-protected topological band with ultracold fermions, Sci. Adv. **4**, eaao4748 (2018).

[53] B. Song, C. He, S. Niu, L. Zhang, Z. Ren, X.-J. Liu, and G.-B. Jo, Observation of nodal-line semimetal with ultracold fermions in an optical lattice, Nat. Phys. **15**, 911 (2019).

[54] N. Q. Burdick, Y. Tang, and B. L. Lev, Long-Lived Spin-Orbit-Coupled Degenerate Dipolar Fermi Gas, Phys. Rev. X **6**, 031022 (2016).

[55] N. Goldman, J. Dalibard, A. Dauphin, F. Gerbier, M. Lewenstein, P. Zoller, and I. B. Spielman, Direct imaging of topological edge states in cold-atom systems, Proc. Natl. Acad. Sci. USA **110**, 6736 (2013).